

# Flexible, biocompatible and highly conductive MXene-graphene oxide film for smart actuator and humidity sensor



Guangwen Jia <sup>a,1</sup>, Ao Zheng <sup>b,1</sup>, Xiao Wang <sup>b</sup>, Lu Zhang <sup>a</sup>, Ling Li <sup>a</sup>, Chenxing Li <sup>a</sup>, Yan Zhang <sup>a,\*</sup>, Lingyan Cao <sup>b,\*</sup>

<sup>a</sup> School of Material Engineering, Shanghai University of Engineering Science, Shanghai 201620, PR China

<sup>b</sup> Department of Prosthodontics, Shanghai Engineering Research Center of Advanced Dental Technology and Materials, Shanghai Key Laboratory of Stomatology & Shanghai Research Institute of Stomatology, National Clinical Research Center for Oral Diseases, Shanghai Ninth People's Hospital, College of Stomatological Sciences, Shanghai Jiao Tong University School of Medicine, Shanghai, China

## ARTICLE INFO

**Keywords:**  
MXene  
Graphene oxide  
Actuator  
Moisture gradient  
Monitoring respiration  
Humidity sensor

## ABSTRACT

The evaporation of water occurs ubiquitously on earth. Hence, smart materials that can directly convert signals generated via water stimulation into mechanical motion have attracted wide attention. However, it is still a challenge to develop novel functional materials with fast response, large scale deformation, and long-term stability for moisture-gradient actuators. Here, a flexible, conductive, layer-structured homogenous  $Ti_3C_2Tx$  MXene-graphene oxide (MGO) film-based moisture-driven actuator and humidity sensor were fabricated. The oxygen groups and d-spacing could be effectively adjusted by MXene/GO composition ratio, thereby tuning the actuation performance.  $MGO_3$  (MXene/GO = 3) displayed a large bending angle, and reversible deformation. And the bending speed of  $MGO_3$  is up to  $32^\circ s^{-1}$ . Furthermore,  $MGO_3$  actuation displayed long-term stability via suppression of MXene oxidation by the introduction of GO and showed good cycling stability.  $MGO_3$  actuators are constructed, which could mimic the blooming of flower, lifting and carrying objects, and be used as a non-contact control switch. In addition, MGO showed a linear sensitive response to humidity and excellent biocompatibility which make it suitable for respiratory monitoring. This work demonstrated that flexible, biocompatibility and conductive MGO films have broad application prospects in the fields of smart actuators, sensing devices, and biology and health care.

## 1. Introduction

Smart soft actuators that can directly convert environment stimuli (humidity [1,2], light [3,4], heat [5], pH [6,7], and magnetic fields [8]) into mechanical movements without an energy supply system have gained significant research interest owing to their potential applications in artificial muscles [9,10], robots [11], sensors [12], and energy generators [13]. Among these, smart actuators driven by a moisture gradient are eco-friendly and easily fabricated; additionally, water is the most abundant resource on earth and evaporation occurs ubiquitously in nature [14], hence, these actuators are considered to be promising for energy conversion. Based on these distinctive properties, the development of smart materials that can directly convert signals generated by water stimulation into kinetic or potential energy is of marked interest [15,16]. To date, various materials have been used to construct smart

actuators, such as carbon-based materials [17], hydrogels [18], polymers [19] and other materials [20]. Despite the significant progress made, further efforts are needed to develop new functional materials for high performance actuators with a fast response, large-scale deformation, and long-term stability.

In recent years, 2D materials have been widely used to develop humidity-responsive actuators. Graphene oxide (GO) and its derivatives with abundant oxygen functional groups are widely studied nanostructured materials [21–23]. They have been demonstrated to possess reversible swelling/shrinking behavior in response to moisture. For example, Ge et al. [24] prepared a homogeneous GO film, which exhibited controllable bending motions. Qiu et al. [25] fabricated a moisture-responsive actuator based on an asymmetric structure. However, the response of the GO film is generally weak, and its insulating characteristics restrict application in intelligent electrical actuators.

\* Corresponding authors.

E-mail addresses: [yanzhang@sues.edu.cn](mailto:yanzhang@sues.edu.cn), [zyecu@126.com](mailto:zyecu@126.com) (Y. Zhang), [cly\\_linya@163.com](mailto:cly_linya@163.com) (L. Cao).

<sup>1</sup> Guangwen Jia and Ao Zheng contribute equally to this work.

Some composite films such as graphene oxide/reduced graphene oxide (GO/rGO) [26,27], graphene oxide/poly (N-isopropylacrylamide) [4], and AgNWs/nanofibers/GO [28] have been synthesized to enhance the properties of moisture actuators. Recently, MXene-based smart materials have been considered to be good potential candidates for fabrication of moisture-gradient actuators. This can be ascribed to the hydrophilic surface and typical layered structure of the MXene, a new 2D material with a general formula  $M_{n+1}X_nT_x$  ( $n = 1, 2, \text{ or } 3$ ), where  $M$  is a transition metal,  $X$  is nitrogen or carbon, and  $T$  represents the surface terminating group (OH, O, or F). The hydrophilic surface, which can be attributed to the functional groups, enables adsorption of water molecules via hydrogen bonding between the OH of the MXene and the water molecules. Additionally, the high conductivity of the MXene makes it feasible for application as an intelligent electrical actuator and sensing. Wang et al. [29] demonstrated that a homogeneous MXene can be used to fabricate highly-conductive smart actuators. Wu et al. [30] prepared  $Ti_3C_2T_x$  MXene based composites for high-performance humidity sensor.  $Ti_3C_2T_x$  MXene also showed high performance for ammonia sensors [31].

However, there are some significant drawbacks that restrict their application in smart actuators. MXene films are weak and brittle because of their relatively weak interflake interactions and the low bending flexibility of the five-atom thick structure [32]. Additionally, MXene films are extremely prone to oxidization to form  $TiO_2$  nanocrystals in aqueous media or under ambient atmosphere [33]. The poor stability of the MXene exposed to an aqueous media or ambient atmosphere can lead to a loss of metallic conductivity and it can also lead to poor adsorption of water [32]. Hence, the long-term stability of MXene-based smart materials is still an open challenge.

In this work, a novel soft actuator with high stability, conductivity, and a quick response to moisture was prepared by combining  $Ti_3C_2T_x$  MXene and GO. The effective contact area would not decrease on mixing GO and MXene, both of which are 2D materials with a large surface area; thereby avoiding a decreased in the moisture responsiveness that would result from a decrease in the effective contact area caused by mixing with other soft composite materials. The homogeneous  $Ti_3C_2T_x$  MXene-graphene oxide (MGO) film showed a large bending angle, fast bending speed, reversible deformation, and good cycling stability in response to a moisture gradient. More importantly, the bending angle of MGO remained nearly unchanged even after 10 days of storage at room temperature ( $\sim 20^\circ\text{C}$ , RH 60 %), while that of  $Ti_3C_2T_x$  MXene decreased to  $0^\circ$ . The long-term stability of the MGO film was significantly improved via the introduction of GO, which could hinder oxygen penetration, and thus, effectively block  $Ti_3C_2T_x$  MXene oxidation. The MGO exhibited a high conductivity, and the resistance of MGO increased with increasing RH because of the swelling effect. Based on these properties, various actuators such as a biomimetic flower, a soft robotic arm, and a non-contact switch were designed and fabricated using the MGO. In addition, MGO showed excellent biocompatibility. It could be used to monitor breathing patterns and respiration rates. Thus, MGO has potential applications as a respiratory monitoring device in the field of portable healthcare and for medical treatment.

## 2. Experimental

### 2.1. Materials

$Ti_3AlC_2$  powder was purchased from 11 Technology Co. Ltd (Jilin, China). Lithium fluoride (LiF), hydrochloric acid (37 %), ethanol (AR, 99.7 %), and mixed fiber membrane (0.22  $\mu\text{m}$ ) were purchased from Aladdin (Shanghai, China). A GO solution was synthesized from natural graphite powder via an improved Hummers' method. Ultrapure water was used in the experiment.

### 2.2. Preparation of $Ti_3C_2T_x$ MXene aqueous

A  $Ti_3C_2T_x$  MXene solution was synthesized according to a previously reported method [34,35]. Briefly, 2 g of lithium fluoride (LiF) and 9 M of hydrochloric acid (HCl) were mixed and stirred for 30 min. Then, 2 g  $Ti_3AlC_2$  was added into the mixture slowly at  $35^\circ\text{C}$  and stirred continuously for 24 h. Then, the samples were washed with ultrapure water until the pH value of the centrifugal supernatant was 6. Ultrapure water was added to the sediment and sonicated for 1 h under  $N_2$  flow. The samples were centrifuged and the supernatant was collected to obtain the  $Ti_3C_2T_x$  solution.

### 2.3. Preparation of the MXene/GO film

Here, 22.5 ml of  $Ti_3C_2T_x$  MXene (2 mg/mL) and 7.5 ml GO (2 mg/mL) solutions were combined under sonication for 15 min to obtain the dispersed composite solution. Then, the mixed solution was filtered with vacuum and dried to form a film. Finally, the film was peeled off and is referred to as  $MGO_3$ . For comparison, the MGO films with a total mass of 30 mg were prepared with various ratios of  $Ti_3C_2T_x$  MXene and GO (1:1, 2:1, and 4:1), and termed as  $MGO_x$ , where  $x$  represented the mass ratio between the MXene and GO. MXene films and GO films were also prepared via the same methods.

### 2.4. Characterization

The surface and cross-sectional morphologies of the  $Ti_3C_2T_x$  MXene and MGO films were observed using scanning electron microscopy (SEM) (Hitachi, S-3400 N, Japan). The chemical structure of the sample was characterized via X-ray energy spectrometry (XPS) (Kratos Analytical, Inc., Manchester, UK). X-ray diffraction (XRD) was carried out using  $Cu K\alpha_1$  (1.5406 Å) radiation and a single-crystal XRD diffractometer (Bruker Advance D8, Germany). Raman spectra were recorded using a Raman spectrometer (French HORIBA Scientific) with a 532 nm laser source. The sheet resistance was characterized by a four-probes testing system (RTS-9, Four Probes Tech Ltd., China). The resistance response was measured using a digital multimeter (Shengli VC890D).

### 2.5. Moisture actuation behaviors

A schematic illustration of the experimental setup is shown in supplementary Fig. S1. The MGO film was cut into a rectangular piece (3 cm  $\times$  1 cm) and placed on a substrate with a rectangular hole in the center, which was used as a window to introduce the vapor gradient. Then, the substrate was placed on a glass container containing water. The moisture gradient can be adjusted via the evaporation rate of water, which can be controlled by changing the water temperature at room temperature ( $\sim 20^\circ\text{C}$ ) and environmental relative humidity  $\sim 60\%$ . The moisture response of the films was recorded with a digital camera. When the film was moved away from water, the moisture gradient disappeared.

### 2.6. Humidity-sensing measurement

The humidity sensing performances of MGO sensor were measured in a custom-made humidity chamber with a controlled relative humidity (RH) value as shown in supplementary Fig. S2. The room temperature and humidity of laboratory were controlled at  $25 \pm 1^\circ\text{C}$  and  $60 \pm 3\%$  RH by an air conditioner. The real-time RH and temperature of humidity chamber were recorded by a thermo-hygrometer. The electrical resistance value of the humidity sensor was measured using a digital multimeter. Phosphorus pentoxide powder ( $P_2O_5$ ) was used as a desiccant to prepare  $3 \pm 1\%$  RH, and the different RH was controlled by the humidifier. The RH response were investigated by exposing the humidity sensor ( $MGO_3$ , 30 mm  $\times$  5 mm) to various RH environments. Then, the  $MGO_3$  humidity sensor was exposed to dry air condition (RH 3 %) to release water molecules. The resistance response is defined as  $\Delta R/R_0 =$

$(R_{RH} - R_0)/R_0 * 100\%$  ( $R_{RH}$  and  $R_0$  are the electrical resistance of films at the given RH and 0% RH, respectively). The time taken by a sensor to achieve 90 % of the total resistance response change was defined as the response or recovery time [36].

## 2.7. Biocompatibility

Biocompatibility of  $Ti_3C_2T_x$  MXene, GO, and  $MGO_3$  samples was evaluated by visible cell reactions of mouse pre-osteoblasts (MC3T3-E1) cells cultured with different membranes. MC3T3-E1 were cultured in basal cell medium (DMEM containing 10 % fetal bovine serum) in a moist environment of 37°C and 5% CO<sub>2</sub>.

The MC3T3-E1 cells suspension with a density of  $1 \times 10^5$  cells/mL was seeded on sterilized  $Ti_3C_2T_x$  MXene, GO, and  $MGO_3$  samples. After 24 h culture, cells were stained with calcein-AM (5 µg/mL) and PI (10 µg/mL), respectively and washed with PBS twice, then imaged using confocal laser-scanning microscopy (CLSM). Meanwhile, the cell adhesion was studied. MC3T3-E1 cells were seeded at a density of  $1 \times 10^5$  cells/mL on different samples, after 24 h incubation, MC3T3-E1 cells were stained with fluorescein isothiocyanate-phalloidin (Sigma, China) and DAPI (Sigma, China), and then observed by CLSM.

CCK-8 assay was carried out for a quantitative analysis on the MC3T3-E1 cells viability. The cells were seeded with a density of  $1 \times 10^5$  cells/mL and cultured on the films at 1 and 4 d. The procedure was carried according to the manufacturer's protocol. Optical density (OD) values of MC3T3-E1 cells were measured at 450 nm to evaluate the proliferation of MC3T3-E1 cells in different samples.

## 3. Results and discussion

### 3.1. Material characterization

$Ti_3C_2T_x$  MXene suspensions were obtained via etching and delamination of  $Ti_3AlC_2$  MAX to remove the Al layers. The SEM and TEM images demonstrate that the MXene sheets are ultrathin and transparent monolayer 2D materials (Fig. 1a-b). The AFM image of GO shows a monolayer sheet with a thickness of ~1.0 nm (Fig. 1c). An  $MGO_3$  suspension was prepared by mixing the  $Ti_3C_2T_x$  MXene and GO suspensions. The Tyndall effect could be observed for the MXene, GO, and  $MGO_3$  suspensions, demonstrating that they had excellent dispersibility (Fig. S3) [37]. Homogenous conductive flexible  $MGO_3$  films were fabricated via simple vacuum filtration of the  $MGO_3$  suspension. The electrical conductivity of  $MGO_3$  was sufficient to illuminate a lamp light (Fig. 1d). The cross-sectional view of  $MGO_3$  demonstrates that the  $MGO_3$  film is ~7.35 µm in thickness, and has a well-ordered layered structure with interlamellar porosity between the layers to facilitate water molecule transportation in the 2D nanochannels (Fig. 1e).

To reveal the structure of  $MGO_3$ , Raman, XRD, and XPS spectroscopies were carried out. In the MXene and  $MGO_3$  spectra, the typical Raman peaks at 198, 283, and 382 cm<sup>-1</sup> could be attributed to the A<sub>1g</sub> vibration peaks of Ti and the Eg group vibrations that include the in-plane (shear) mode of Ti and C, respectively (Fig. 1f) [38]. Additionally, two distinct peaks at 1335 and 1596 cm<sup>-1</sup> corresponding to the D and G bands of GO were observed in the spectrum of  $MGO_3$  (Fig. 1f) [39]. The coexistence of the characteristic  $Ti_3C_2T_x$  MXene and GO peaks in the  $MGO_3$  films revealed that GO and  $Ti_3C_2T_x$  MXene successfully combined in the composite film. The XRD pattern of  $Ti_3C_2T_x$  MXene exhibited a sharp peak (002) at  $2\theta = 6.76^\circ$ , corresponding to a d-spacing

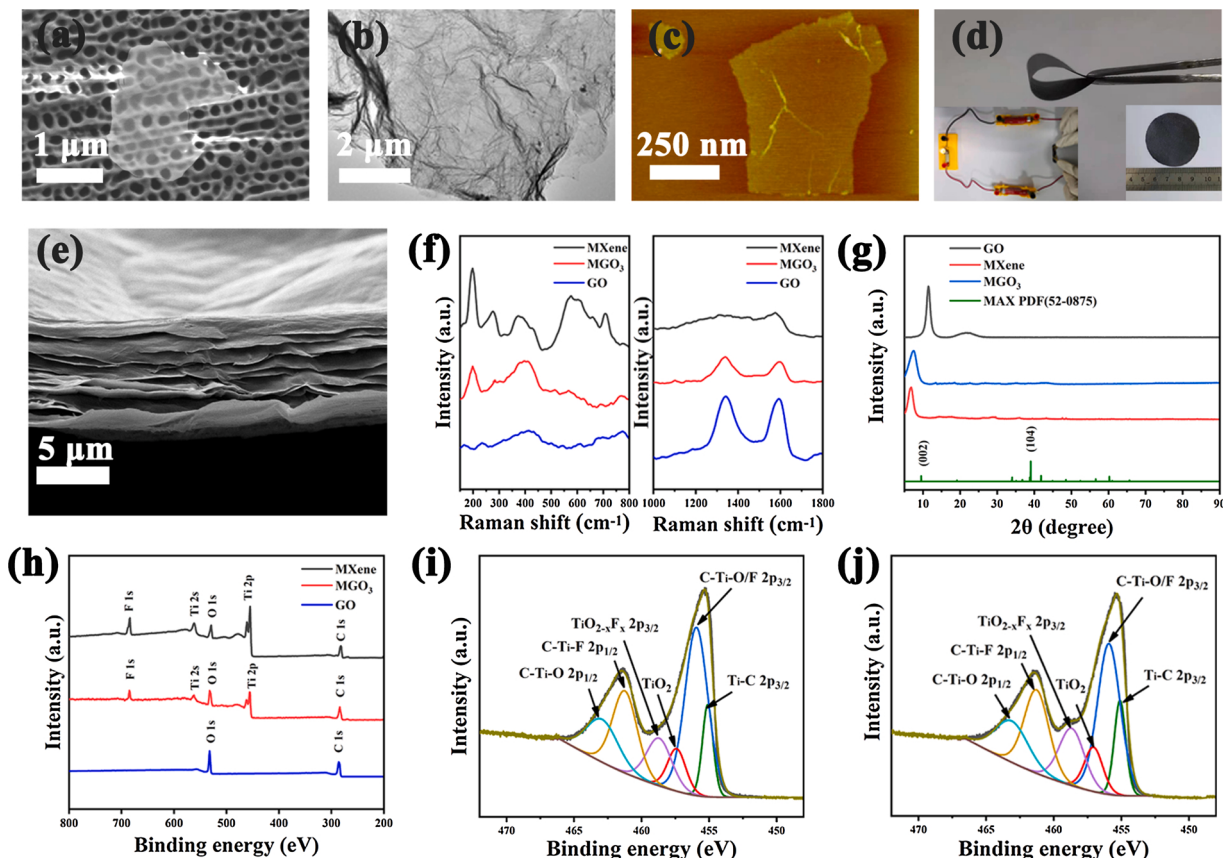


**Fig. 1.** (a) SEM and (b) TEM images of MXene. (c) AFM image of GO. (d) Optical of  $MGO_3$  film. Inset: the electroconductive  $MGO_3$  closed the circuit and the lamp lit up. (e) SEM cross-section images of  $MGO_3$  film. (f) Raman spectra and (g) XRD patterns of pure MXene, GO, and  $MGO_3$  film. (h) XPS spectra of pure MXene and  $MGO_3$ . (i) and (j) Ti 2p XPS spectra of MXene and  $MGO_3$ , respectively.

of  $12.99\text{ \AA}$ , and this demonstrated the successful removal of Al from the  $\text{Ti}_3\text{AlC}_2$  MAX phase (Fig. 1g) [40]. The XRD profile of GO exhibited a sharp peak at  $2\theta = 11.5^\circ$ , corresponding with a d-spacing of  $7.70\text{ \AA}$ . In the XRD pattern of  $\text{MGO}_3$ , the GO peak disappeared and the  $\text{Ti}_3\text{C}_2\text{T}_\text{X}$  MXene peak shifted to  $7.65^\circ$ , corresponding to a d-spacing of  $11.77\text{ \AA}$ . The results are similar to those reported in literature [41,42]. It should be noted that no  $\text{TiO}_2$  peak was observed in the XRD patterns for  $\text{Ti}_3\text{C}_2\text{T}_\text{X}$  MXene and  $\text{MGO}_3$ .

The chemical composition of the films was further analyzed using X-ray photoelectron spectroscopy (XPS). As shown in Fig. 1h, four main elements (C, Ti, O, and F) were present in  $\text{Ti}_3\text{C}_2\text{T}_\text{X}$  MXene and  $\text{MGO}_3$ , indicating that etching the MAX phase with LiF resulted in OH, O, and F MXene surface termination [40]. The oxygen content of  $\text{Ti}_3\text{C}_2\text{T}_\text{X}$  MXene, GO, and  $\text{MGO}_3$  were 15.07 %, 26.9 % and 21.13 %, respectively.  $\text{MGO}_3$  had a higher content of O than that of  $\text{Ti}_3\text{C}_2\text{T}_\text{X}$  MXene because of the introduction of GO. Literature pointed out that epoxide, carboxyl, and hydroxyl functional groups can effectively attract water molecules onto the surface of the GO sheets to form a dense hydrogen-bonding network [43]. Thus, these oxygen elements of  $\text{MGO}_3$  provided abundant adsorption sites for water molecules. The high-resolution Ti (2p) spectra of  $\text{Ti}_3\text{C}_2\text{T}_\text{X}$  MXene and  $\text{MGO}_3$  can be deconvoluted into six peaks at 455.1, 455.9, 457.4, 458.7, 461.2, and 463.0 eV, corresponding to  $\text{Ti}-\text{C}$   $2\text{p}_{3/2}$ ,  $\text{CTiO}—/\text{F}$   $2\text{p}_{3/2}$ ,  $\text{TiO}_2$ ,  $\text{Ti}_{2-x}\text{F}_x$   $2\text{p}_{3/2}$ ,  $\text{C}-\text{TiF}$   $2\text{p}_{1/2}$ , and  $\text{CTiO}—$   $2\text{p}_{1/2}$ , respectively (Fig. 1i and j) [44]. The  $\text{TiO}_2$  peak was the weakest and the intensity of  $\text{MGO}_3$  remained unchanged compared with that of the  $\text{Ti}_3\text{C}_2\text{T}_\text{X}$  MXene, indicating a very small amount of  $\text{Ti}_3\text{C}_2\text{T}_\text{X}$  MXene was oxidized and no further oxidation occurred during  $\text{MGO}_3$  processing.

The biocompatibility of smart materials is an essential factor for biological, medical and health applications. In this study, cell attachment was analyzed by cell adhesion assays. Fig. 2a shows CLSM images of cytoskeleton morphology stained by FITC and DAPI after MC3T3-E1 cells were cultured on MXene, GO and  $\text{MGO}_3$  samples for 24 h. MC3T3-E1 cells were found to be attached to the surface of all samples. And no significant differences of the cell's morphology on the surface of

$\text{GO}$ ,  $\text{Ti}_3\text{C}_2\text{T}_\text{X}$  MXene and  $\text{MGO}_3$  films were noted. The results indicated that the films have potential for cell adhesion. To evaluate cell viability of the films, we stained the cells with a live/dead staining kit. The fluorescent images of MC3T3-E1 cells after co-cultured with samples for 24 h are shown in Fig. 2b. The green fluorescence indicated the live cells while red fluorescence indicated the dead ones. A large number of live cells (green) and few dead cells (red) on  $\text{GO}$ , MXene and  $\text{MGO}_3$  films were observed, confirming a good biocompatibility of the materials. Fig. 2c shows the OD value of cck-8 test of MC3T3-E1 cells culturing on  $\text{Ti}_3\text{C}_2\text{T}_\text{X}$  MXene, GO and  $\text{MGO}_3$  samples. On day 1, there was no significant difference in OD value among  $\text{Ti}_3\text{C}_2\text{T}_\text{X}$  MXene, GO and  $\text{MGO}_3$ . After 4 days of growth, all the samples showed higher OD than those after 1 day of growth except  $\text{Ti}_3\text{C}_2\text{T}_\text{X}$  MXene groups, suggesting that cells on GO and  $\text{MGO}_3$  were in proliferation. Furthermore, the OD value of cells on  $\text{MGO}_3$  was significantly higher than that of the control groups and the other groups. The results showed that  $\text{MGO}_3$  has excellent biocompatibility.

### 3.2. Moisture actuation behaviors

The actuation behavior of the homogeneous  $\text{MGO}_3$  films upon exposure to a moisture gradient were investigated at  $20 \pm 1^\circ\text{C}$  and  $60 \pm 3\%$  RH. As shown in Fig. 3a, when the  $\text{MGO}_3$  film was held on the palm of a hand (Video S1), it curved up and flipped, while it remained flat on the dry surface of a gloved palm, which eliminated thermally-induced actuation. Furthermore, when the  $\text{MGO}_3$  film was placed in a closed space with a RH of up to 90 %, it retained its initial shape and showed no locomotion (Fig. S4). The above phenomena indicated that the deformation of the  $\text{MGO}_3$  film was triggered by a moisture gradient, which is in agreement with previous reports on pure MXene [29] and pure GO films [24]. When approaching the  $\text{MGO}_3$  film with a fingertip without making contact (Fig. 3b), a significant downward-bending of  $\text{MGO}_3$  films could be observed, indicating that the  $\text{MGO}_3$  film was very sensitive to a moisture gradient. In addition, when the  $\text{MGO}_3$  film was placed on a humid substrate at  $40^\circ\text{C}$ , it flipped in the regular manner (Fig. 3c)

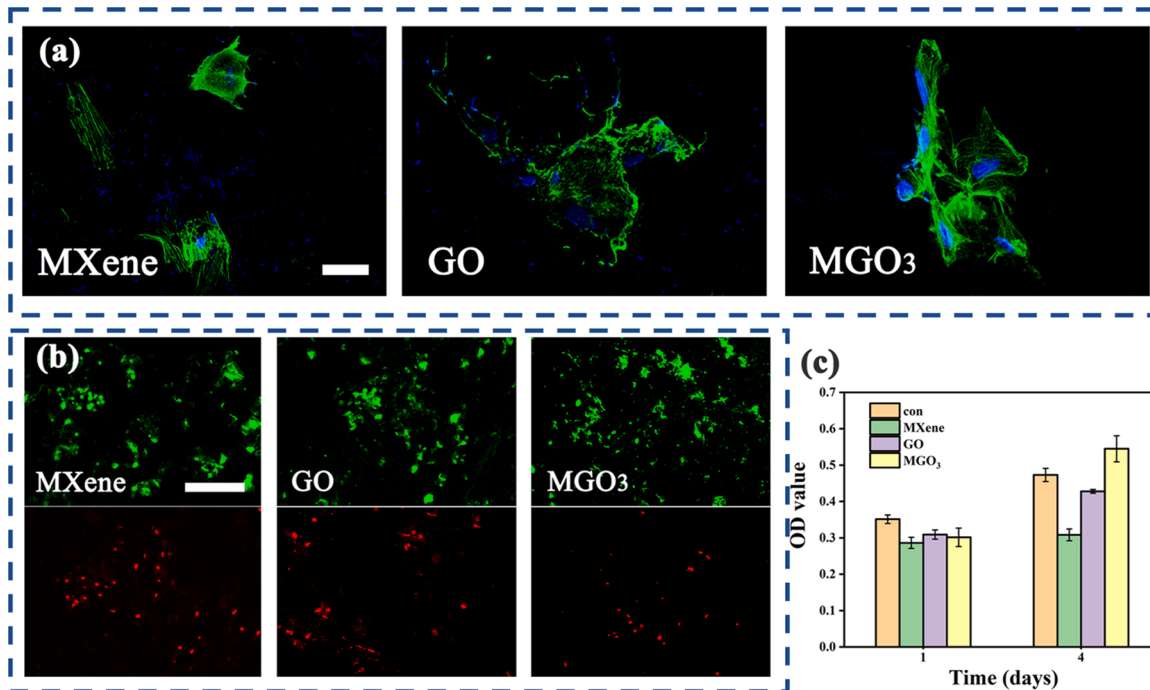


**Fig. 2.** (a) Cell attachment and morphology of MC3T3-E1 cells on MXene, GO, and  $\text{MGO}_3$  for 24 h of culture (bar =  $50\text{ }\mu\text{m}$ ). (b) Cell viability of MC3T3-E1 cells on MXene, GO, and  $\text{MGO}_3$  films; the fluorescent images of live (green) and dead (red) MC3T3-E1 cells cultured for 24 h (Scale bars =  $250\text{ }\mu\text{m}$ ). (c) OD value of MC3T3-E1 cells cultured on MXene, GO and  $\text{MGO}_3$  for different time. (For interpretation of the references to colour in this figure legend, the reader is referred to the web version of this article).

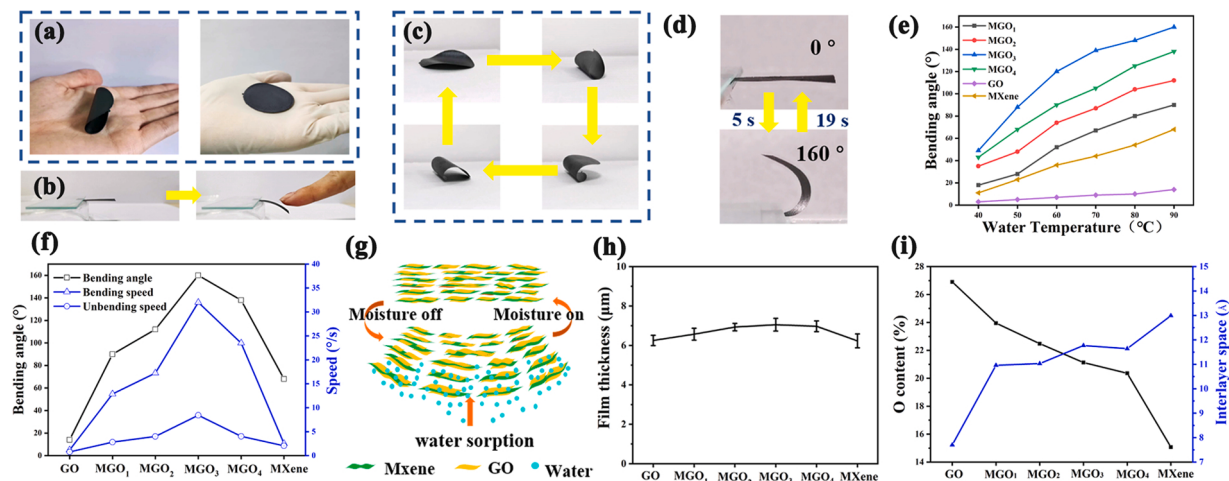


**Fig. 3.** (a) MGO<sub>3</sub> exhibited different behavior in response to human sweat when placed on a palm with and without a glove. (b) Downward bending of the MGO<sub>3</sub> film was observed when the fingertip approached. (c) The switching process of the MGO<sub>3</sub> film on a humid substrate. (d) Bending/recovery process of the MGO<sub>3</sub> film. (e) The maximum bending angle of the GO, MGOx, and MXene films at various water temperatures. (f) The maximum bending angles and bending/recovery speeds of the GO, MGOx, and MXene films. (water temperature = 90 °C, RH = 60 %). (g) Schematic diagram of the bending mechanism. (h) The thickness of the GO, MGOx, and MXene films. (i) O content and interlayer spacing of GO, MGOx, and MXene films.

and Video S2). When the MGO<sub>3</sub> film was placed on the humid substrate, the bottom surface of the film contacted the substrate and absorbed more water molecules than the top surface, resulting in a bending deformation caused by asymmetric expansion. Then, the center of mass of the MGO film moved upwards and gradually reached the critical position, where the film became mechanically unstable and turned over. Thereafter, the MGO<sub>3</sub> film extended because of water desorption from the top surface of the film and water adsorption at the film/substrate interface. Eventually, most of the contact area bent up, and the film fell back to the substrate and began a new cycle. The deformation process triggered by the moisture gradient could flip over six times in 1 min with no sign of fatigue. This demonstrated that the MGO<sub>3</sub> film facilitated moisture induced actuation.

To further quantitatively analyze the actuation behavior triggered by a moisture gradient, a testing device was designed, as shown in Fig. S1. A film (3 cm × 1 cm) was placed on a substrate with a rectangular hole in the center that functioned as a window to introduce a vapor gradient at room temperature (~20°C) and environmental RH ~60 %. When the bottom surface of the MGO<sub>3</sub> film faced the water vapor (water temperature = 90°C), the bending angle increased to 160° within ~5 s. Then, it returned to its initial flat state with 19 s, when the film was moved away from the water vapor (Fig. 3d). The effect of the Ti<sub>3</sub>C<sub>2</sub>T<sub>x</sub> MXene/GO ratio on the film's actuating properties was further investigated. At a constant ambient humidity, the moisture gradient could be adjusted via the evaporation rate of water, which was controlled by changing the water temperature. On increasing the Ti<sub>3</sub>C<sub>2</sub>T<sub>x</sub> MXene/GO ratio, the maximum bending angle of the films initially increased and then decreased at similar water temperatures; a higher temperature resulted in a larger bending deformation (Figs. S5 and 3 e). Furthermore, the bending angle, bending speed, and recovery speed also initially increased and then decreased with increasing Ti<sub>3</sub>C<sub>2</sub>T<sub>x</sub> MXene/GO ratio, and reached their maximum values at MXene/GO = 3 (Figs. 3f and S6; water temperature = 90°C, RH = 60 %). The bending angle of MGO<sub>3</sub> was approximately 2-fold and 11-fold higher than that of MXene and GO, respectively. The bending speed of MGO<sub>3</sub> was approximately 12-fold and 18-fold higher than that of MXene and GO respectively. Compared with most reported actuators, MGO<sub>3</sub> displayed a faster bending (32°·s<sup>-1</sup>) and unbending speed (8°·s<sup>-1</sup>) (Table S1).

The homogeneous-film actuator was triggered by a moisture gradient as previously indicated. Once the bottom surface of MGO was in contact with the vapor molecules, the bottom layer adsorbed the water molecules and expanded because of the strong hydrogen bonds formed

between the oxygen functional groups of MGO and the water molecules (Fig. 3g). It was noted that GO was able to resist water vapor permeation [45]. Thus, the ordered lamellar structure and oxygen functional groups of the internal film could form a high-friction capillary channel and delay the transportation of water molecules, resulting in a swelling difference in the vertical direction [46,47]. A gradient of water in the internal film enhanced the bending moment. As a result, the MGO film curved away from the bottom surface toward the top surface. To further understand the curving mechanism triggered by a moisture gradient, SEM, XPS and XRD analysis were carried out on the GO, MGOx, and MXene films. With increasing Ti<sub>3</sub>C<sub>2</sub>T<sub>x</sub> MXene content, the average film thickness varied insignificantly (Figs. 3h and S7). So, the effect of thickness on the actuation performance could be ignored. As shown in Figs. 3i and S8, because of the low oxygen content of the Ti<sub>3</sub>C<sub>2</sub>T<sub>x</sub> MXene, the O content decreased with introduction of the Ti<sub>3</sub>C<sub>2</sub>T<sub>x</sub> MXene, resulting in weak hydrogen bonding with the water molecules and a low-friction capillary channel. From this perspective, a high content of Ti<sub>3</sub>C<sub>2</sub>T<sub>x</sub> MXene is detrimental to the actuation performance. However, analysis of the XRD results shows that on increasing the Ti<sub>3</sub>C<sub>2</sub>T<sub>x</sub> MXene content, the peaks for GO in MGO disappeared and the d-spacing of MGO increased, suggesting that the stacking of the GO layers were broken with the introduction of the Ti<sub>3</sub>C<sub>2</sub>T<sub>x</sub> MXene sheets (Figs. 3i and S9). A larger interlayer spacing results in a larger surface area and more porous structure that leads to a rapid adsorption/desorption rate for the water molecules [28]. Thus, a comprehensive analysis was carried out that took into account the influence of factors such as the oxygen content and interlayer spacing on the actuation performance in response to a moisture gradient. The results demonstrated that MGO<sub>3</sub> is a promising smart material.

The stability of the composite films is a critical issue for practical applications. The stability of the GO, Ti<sub>3</sub>C<sub>2</sub>T<sub>x</sub> MXene, and MGO<sub>3</sub> films (0.5 cm × 0.5 cm) were evaluated in water (Fig. S10). It was found that when they came in contact with water, the Ti<sub>3</sub>C<sub>2</sub>T<sub>x</sub> MXene film dissolved and formed a dispersion immediately, and after shaking, the GO completely fragmented. This could be attributed to the high electrostatic repulsion, relative to the π-π attraction of GO, which is due to the abundant oxygen functional groups [47] and the relatively weak van der Waals forces between neighboring sheets in the five-atom-thick MXene structure [32]. After 2 months, the Ti<sub>3</sub>C<sub>2</sub>T<sub>x</sub> MXene sample was clear and colorless while the MGO<sub>3</sub> film remained intact in water, indicating high stability of MGO<sub>3</sub> in this environment. This discrepancy could be attributed to the strong hydrogen bonds between the Ti<sub>3</sub>C<sub>2</sub>T<sub>x</sub> MXene

and GO sheets, and the decreased electrostatic repulsion because of the low oxygen group content. To further study their stability under ambient conditions, the  $\text{Ti}_3\text{C}_2\text{T}_{\text{x}}$  MXene and  $\text{MGO}_3$  films were stored at 20°C, RH = 60 % and tested using the moisture gradient testing apparatus (water temperature = 90°C, RH = 60 %). After 10 days, it was found that the  $\text{Ti}_3\text{C}_2\text{T}_{\text{x}}$  MXene film no longer had moisture-driven actuation, while the bending angle of the  $\text{MGO}_3$  film was still maintained 155° (Fig. 4a). The long-term stability of the  $\text{MGO}_3$  film with a moisture-gradient actuation was again found to be superior to that of the  $\text{Ti}_3\text{C}_2\text{T}_{\text{x}}$  MXene actuator.

To explore the structure of the  $\text{Ti}_3\text{C}_2\text{T}_{\text{x}}$  MXene and  $\text{MGO}_3$  films after 10 days of storage, XRD and XPS were carried out. As shown in Fig. 4b, new peaks located at 25.4°, 37.8°, 47.5°, and 75.8° that correspond with the anatase phase of  $\text{TiO}_2$  (JCPDS card 00-021-1272) appeared in the XRD pattern of  $\text{Ti}_3\text{C}_2\text{T}_{\text{x}}$  MXene. Meanwhile, no peaks associated with  $\text{TiO}_2$  were observed in the XRD results for  $\text{MGO}_3$ . These results were further confirmed via XPS analysis. The Ti 2p XPS spectrum of  $\text{Ti}_3\text{C}_2\text{T}_{\text{x}}$  MXene showed that the  $\text{TiO}_2$  content doubled compared with the fresh MXene (Figs. 4c and 1 i). However, the XPS spectrum of  $\text{MGO}_3$  showed no distinct changes compared with the fresh film (Figs. 4d and 1 h). The elemental composition and structure of  $\text{MGO}_3$  were both well preserved, which may explain the long-term stability of  $\text{MGO}_3$ . These results suggested that the stability of the  $\text{Ti}_3\text{C}_2\text{T}_{\text{x}}$  MXene film can be greatly enhanced by coating the GO sheets, which can hinder the penetration of oxygen inside the film and effectively block  $\text{Ti}_3\text{C}_2\text{T}_{\text{x}}$  MXene oxidation (Fig. 4e). Thus, the improvement in the long-term stability of MGO can be explained by its antioxidant properties. Homogenous  $\text{MGO}_3$  films that are based on the same materials are expected to have a strong mechanically coherent interface. After testing over 50 bending-recovery cycles via exposure to a moisture gradient (water temperature = 90°C, RH = 60 %), the maximum bending angle remained essentially unchanged and the film could also return to the initial flat state (Fig. 4f). The bending and unbending deformation of the  $\text{MGO}_3$  were highly reversible, indicating that the  $\text{MGO}_3$  actuator had good cycling stability.

### 3.3. Actuator application

The outstanding moisture-response, excellent conductivity, and high stability of the flexible  $\text{MGO}$  film makes it promising for fabricating smart biomimetic soft actuators. As shown in Fig. 5a, a bionic flower

with six petals was designed and manufactured. By introducing water vapor with a plastic straw, the bionic flower bloomed and reached its maximum expansion within 16 s. With the removal of the water vapor source, the flower gradually closed (Video S3). Then, a robotic arm was designed based on the bending actuation of the  $\text{MGO}$  film triggered by a moisture gradient, as shown in Fig. 5b and Video S4. When the  $\text{MGO}_3$  film was close to the humid substrate, it quickly bent upward and lifted an object several times heavier than itself. Then, the object was moved and released to a dry substrate. It was notable that the application of the  $\text{MGO}_3$  film was not limited to these operations. Owing to its good electrical conductivity, the  $\text{MGO}$  film was also applied as a “non-contact switch.” As shown in Fig. 5c and Video S5, one side of  $\text{MGO}_3$  film was connected with the circuit and the other side could be controlled to touch the circuit and light up a small lamp on approach with a fingertip. When the fingertip was removed, the  $\text{MGO}_3$  film returned to its original state, and thus, the circuit was disconnected and the lamp was switched off.

### 3.4. Humidity sensor

The electrical conductivity of smart material is very important for the development and application of smart devices, and the application of GO would be severely limited by its insulating properties. However, because of the excellent conductivity of  $\text{Ti}_3\text{C}_2\text{T}_{\text{x}}$  MXene sheets, the sheet resistance of the  $\text{MGO}_x$  films decreased rapidly with increasing  $\text{Ti}_3\text{C}_2\text{T}_{\text{x}}$  MXene content (Fig. 6a). Thus, the resistance of the  $\text{MGO}_x$  film can be easily controlled. The sheet resistance of the  $\text{MGO}_3$  film was 9.7 ohm/sq, indicating high electrical conductivity. The resistance response ( $\Delta R/R_0$ ) of  $\text{MGO}_x$  with RH was evaluated. Compared with MXene film and other  $\text{MGO}_x$  film (Fig. S11), the  $\text{MGO}_3$  with the ability to rapid adsorption and desorption of water molecules showed higher response to humidity due to abundant of hydrophilic functional groups and high electrical conductivity, indicating that  $\text{MGO}_3$  is expected as a potential candidate for humidity sensing material. As shown in Fig. 6b, the  $\text{MGO}_3$  sensor exhibited a positive humidity coefficient of resistance. The average resistance response of  $\text{MGO}_3$  sensor increased linearly with increasing RH, and the maximum response at 90 % RH was calculated to be 107.58 %. The corresponding linear function is  $\Delta R/R_0 = 1.151RH - 1.044$  ( $R^2 = 0.9904$ ) with a wide range of 3 %–90 % RH. Fig. 6c shows the continuous

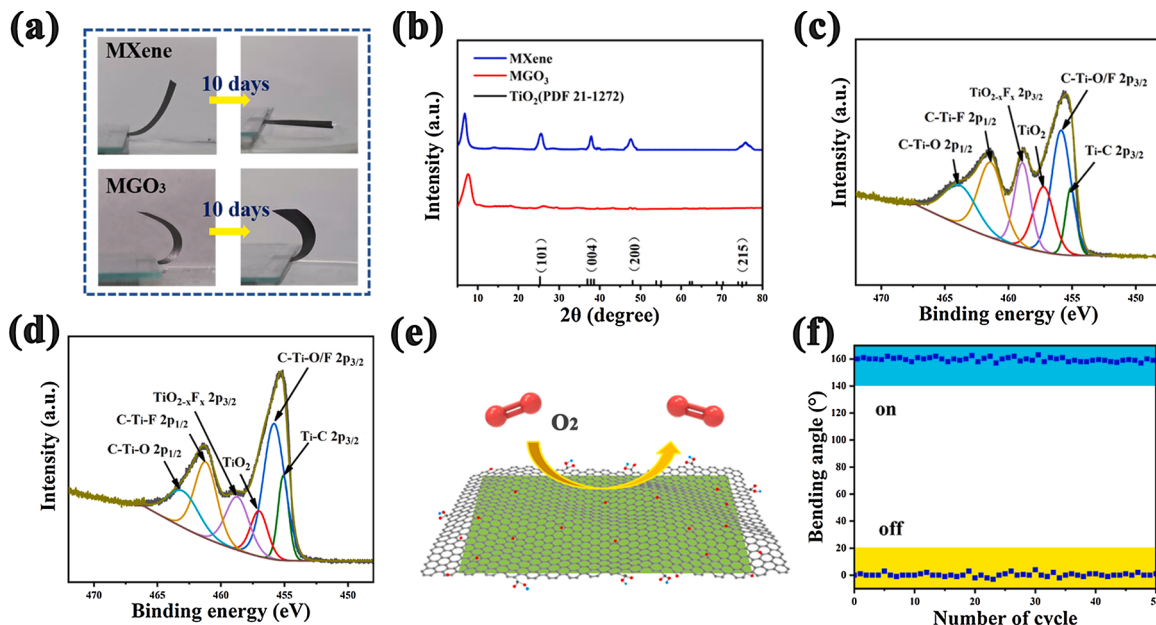


**Fig. 4.** (a) Moisture gradient driven bending angle of the MXene and  $\text{MGO}_3$  after 10 days at 25 °C, RH = 60 % (water temperature = 90 °C). (b) XRD patterns of the MXene and  $\text{MGO}_3$  films after 10 days. (c-d) Ti 2p XPS spectra of MXene (c) and  $\text{MGO}_3$  (d) films stored for 10 days under ambient conditions. (e) Schematic diagram of the  $\text{MGO}$  film preventing oxidation. (f) The reversible bending/recovery properties of the  $\text{MGO}_3$  film over 50 cycles. (water temperature = 90 °C, RH = 60 %).

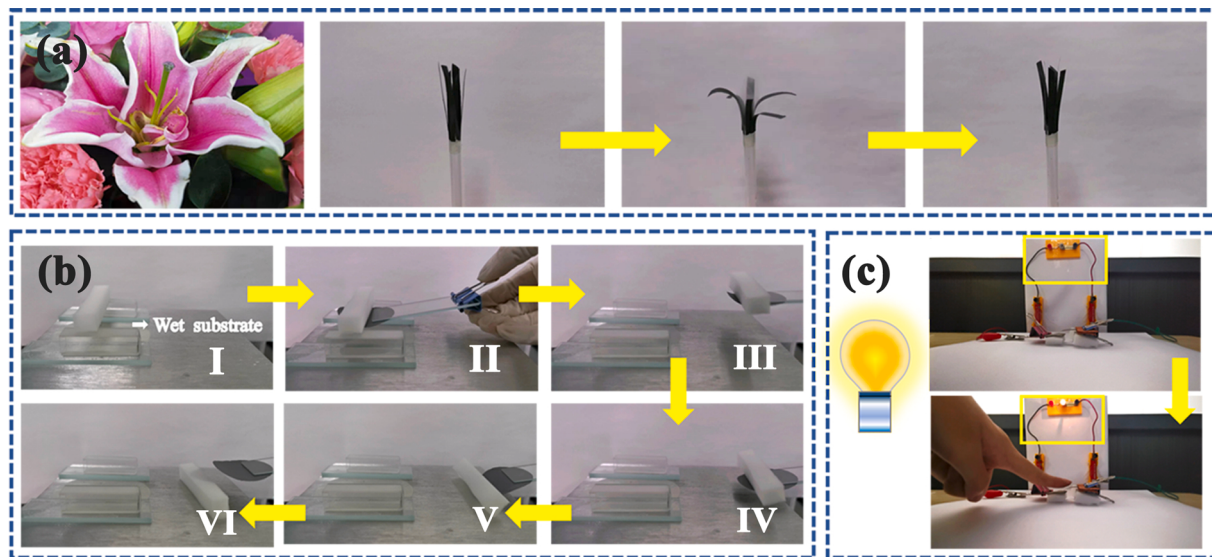


**Fig. 5.** Biomimetic application of the  $\text{MGO}_3$  Film. (a) Blooming and closure of the bionic flower prepared using the  $\text{MGO}_3$  film driven by moisture. (b)  $\text{MGO}_3$  film simulates a robotic arm lifting and moving object via a moisture gradient. (c) smart non-contact switch triggered by a fingertip.

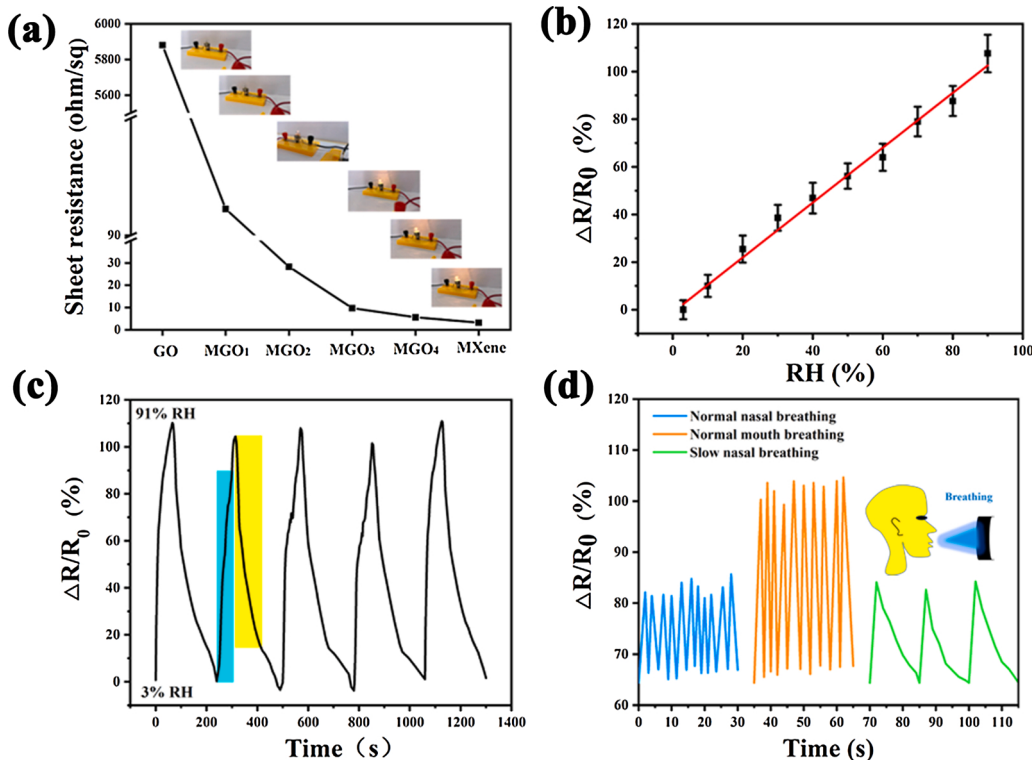


**Fig. 6.** (a) The sheet resistance of the GO,  $\text{MGO}_x$ , and MXene films. (b) Resistance response of the  $\text{MGO}_3$  film with different RH values. (c) Dynamic responses of the  $\text{MGO}_3$  sensor between 3% RH and 91% RH in 5 repeated sensing cycles. (d) Resistance response of the  $\text{MGO}_3$  film under oral and nasal respiration.

response and recovery curves of the humidity sensor between 3% RH and 91% RH, indicating a good reproducibility for the  $\text{MGO}_3$  humidity sensor. The response and recovery times of  $\text{MGO}_3$  humidity sensor were 58 s and 104 s, respectively, which are smaller than those of other carbon-based humidity sensor (Fig. 6c and Table S2). The hysteresis characteristic was also measured in 3–80% RH range (Fig. S12). The moisture adsorption-desiccation responses had a good coincidence degree with the maximal hysteresis of 5.5% at 60% RH (Fig. S12). These results demonstrated that the  $\text{MGO}_3$  humidity sensor had good humidity sensing performance.

According to previous reported [12], the possible humidity mechanism of  $\text{MGO}_3$  sensor is expressed as follows. Generally, the positive humidity sensing property of carbon materials humidity sensors is attributed to the swelling effect of material adsorbed water molecules. Water molecules are physically adsorbed on the  $\text{Ti}_{3}\text{C}_2\text{Tx}$  MXene and GO surface, and will partially dissociate to produce  $\text{H}_3\text{O}^+$  as charge carrier by Grothuss chain reaction. However, compared with high conductive MXene, the effect of promoting conduction is negligible [48]. At low RH, the electron tunneling would be hindered by adsorbed water molecular membrane on the surface of MXene, so the resistance of  $\text{MGO}_3$  sensor

increased with increasing RH. At high RH, the swelling of  $\text{MGO}_3$  with the adsorption of a large number of water molecules enhanced the space between MXene and reduced the degree of connectivity, resulting in increased resistance with the increase of RH [49]. The equilibration of system was reached when the swelling effect of  $\text{MGO}$  reached saturation. In general, the “swelling effect” can be considered as a primary sensing mechanism, and this demonstrates that  $\text{MGO}_3$  has potential for application as a humidity sensor.

In recent years, respiration monitoring has become a significant part of clinical diagnostics and disease monitoring, including for applications such as anti-choking, respiration monitoring, and sleep apnea treatment [34].  $\text{MGO}_3$  displayed good biocompatibility and its humidity sensing performance makes it an ideal choice for use as a human respiration monitor that can realize continuous and long-term monitoring for changes in vital signs. As a proof of concept, a human respiration monitoring device was constructed using an  $\text{MGO}_3$  film (Fig. 6c). Because of the release of increased moisture during breathing via the mouth, the  $\text{MGO}_3$  response is much higher during this process than for nasal breathing. The fabricated  $\text{MGO}$  sensor could not only differentiate between breathing patterns, but also monitor the respiration rates. The response frequency was recorded via the response-time curves and the response time of  $\text{MGO}_3$  was less than 1.07 s. Because of its excellent biocompatibility, the multi-functional integrated intelligent  $\text{MGO}_3$  film has potential application as a respiration monitoring device for portable healthcare and medical treatment.

#### 4. Conclusion

In this work, conductive-film-based flexible actuators triggered via a moisture gradient were prepared by combining  $\text{Ti}_3\text{C}_2\text{T}_{\text{x}}$  MXene and GO. The oxygen content and interlayer spacing which could be adjusted via the  $\text{Ti}_3\text{C}_2\text{T}_{\text{x}}$  MXene/GO ratio, could contribute to the actuation performance in response to a moisture gradient. The  $\text{MGO}_3$  film exhibited a large bending deformation, fast response, and reversible actuation in response to the presence or absence of moisture. GO could prevent the oxidation of the  $\text{Ti}_3\text{C}_2\text{T}_{\text{x}}$  MXene, thus, improving the long-term stability of  $\text{MGO}$ . Additionally, the conductive  $\text{MGO}$  exhibited a high resistance response to RH. A series of applications were designed to confirm the potential of  $\text{MGO}$  for application in actuators and sensor. A simulated flower, robotic arm, and non-contact switch were successfully fabricated. Furthermore, the  $\text{MGO}$  film exhibited excellent biocompatibility and humidity sensing which enabled its use for respiration monitoring. This research could promote the application of biomimetic films driven via a moisture gradient for various applications, including in soft robotics and sensors.

#### CRediT authorship contribution statement

Guangwen Jia: Methodology, investigation, writing-original draft preparation.

Ao Zheng: Methodology, investigation, part of writing-original draft preparation.

Xiao Wang: Investigation.

Lu Zhang: Validation.

Ling Li: Validation.

Chenxing Li: Validation.

Yan Zhang: Conceptualization, writing-review & editing, supervision, funding acquisition.

Lingyan Cao: Conceptualization, Writing-review & editing.

#### Declaration of Competing Interest

The authors declare that they have no competing interests.

#### Acknowledgement

This work was supported by the National Natural Science Foundation of China (Grant No. 51602192).

#### Appendix A. Supplementary data

Supplementary material related to this article can be found, in the online version, at doi:<https://doi.org/10.1016/j.snb.2021.130507>.

#### References

- [1] G. Xu, J. Chen, M. Zhang, G. Shi, An ultrasensitive moisture driven actuator based on small flakes of graphene oxide, *Sens. Actuators B Chem.* 242 (2017) 418–422.
- [2] Q. Chen, X. Yan, H. Lu, N. Zhang, M. Ma, Programmable polymer actuators perform continuous helical motions driven by moisture, *ACS Appl. Mater. Interfaces* 11 (2019) 20473–20481.
- [3] M.N. Muralidharan, K.P. Shinu, A. Seema, Optically triggered actuation in chitosan/reduced graphene oxide nanocomposites, *Carbohydr. Polym.* 144 (2016) 115–121.
- [4] Z. Chen, R. Cao, S. Ye, Y. Ge, Y. Tu, X. Yang, Graphene oxide/poly (N-isopropylacrylamide) hybrid film-based near-infrared light-driven bilayer actuators with shape memory effect, *Sens. Actuators B Chem.* 255 (2018) 2971–2978.
- [5] L. Guo, Y.-W. Hao, P. Yang, P.-L. Li, N. Sun, X.-W. Feng, J. Zhao, C.-A. Chen, J.-F. Song, Fast fabrication of graphene oxide/reduced graphene oxide hybrid hydrogels for thermosensitive smart actuator utilizing laser irradiation, *Mater. Lett.* 237 (2019) 245–248.
- [6] Y. Cheng, K. Ren, D. Yang, J. Wei, Bilayer-type fluorescence hydrogels with intelligent response serve as temperature/pH driven soft actuators, *Sens. Actuators B Chem.* 255 (2018) 3117–3126.
- [7] B. Wu, X. Le, Y. Jian, W. Lu, Z. Yang, Z. Zheng, P. Théato, J. Zhang, A. Zhang, T. Chen, pH and thermo dual-responsive fluorescent hydrogel actuator, *Macromol. Rapid Commun.* 40 (2019), e1800648.
- [8] Z. Zhang, X. Li, X. Yu, H. Chai, Y. Li, H. Wu, S. Jiang, Magnetic actuation bionic robotic gripper with bistable morphing structure, *Compos. Struct.* 229 (2019), 111422.
- [9] M.R.A. Bhatti, E. Bilotti, H. Zhang, S. Varghese, R.C.P. Verpaalen, A.P.H. J. Schenning, C.W.M. Bastiaansen, T. Peijls, Ultra-high actuation stress polymer actuators as light-driven artificial muscles, *ACS Appl. Mater. Interfaces* 12 (2020) 33210–33218.
- [10] M.P.M. Dicker, A.B. Baker, R.J. Iredale, S. Naficy, I.P. Bond, C.F.J. Faul, J. M. Rossiter, G.M. Spinks, P.M. Weaver, Light-triggered soft artificial muscles: molecular-level amplification of actuation control signals, *Sci. Rep.* 7 (2017) 9197.
- [11] Y. Dong, J. Wang, X. Guo, S. Yang, M.O. Ozen, P. Chen, X. Liu, W. Du, F. Xiao, U. Demirci, B.-F. Liu, Multi-stimuli-responsive programmable biomimetic actuator, *Nat. Commun.* 10 (2019) 4087.
- [12] Q. Zhao, Z. Yuan, Z. Duan, Y. Jiang, X. Li, Z. Li, H. Tai, An ingenious strategy for improving humidity sensing properties of multi-walled carbon nanotubes via poly-L-lysine modification, *Sens. Actuators B Chem.* 289 (2019) 182–185.
- [13] T. Yang, H. Yuan, S. Wang, X. Gao, H. Zhao, P. Niu, B. Liu, B. Li, H. Li, Tough biomimetic films for harnessing natural evaporation for various self-powered devices, *J. Mater. Chem. A* 8 (2020) 19269–19277.
- [14] Y. Park, X. Chen, Water-responsive materials for sustainable energy applications, *J. Mater. Chem. A* 8 (2020) 15227–15244.
- [15] J. Duan, F. Liu, Y. Kong, M. Hao, J. He, J. Wang, S. Wang, H. Liu, Y. Sang, Homogeneous chitosan/graphene oxide nanocomposite hydrogel-based actuator driven by efficient photothermally induced water gradients, *ACS Appl. Nano Mater.* 3 (2020) 1002–1009.
- [16] X. Wang, H. Zhang, X. Liu, A free-standing carbon nitride actuator is driven by the ambient humidity, *Diam. Relat. Mater.* 97 (2019), 107434.
- [17] W. Wang, C. Xiang, Q. Zhu, W. Zhong, M. Li, K. Yan, D. Wang, Multistimulus responsive actuator with GO and carbon nanotube/PDMS bilayer structure for flexible and smart devices, *ACS Appl. Mater. Interfaces* 10 (2018) 27215–27223.
- [18] Y. Tan, D. Wang, H. Xu, Y. Yang, W. An, L. Yu, Z. Xiao, S. Xu, A fast, reversible, and robust gradient nanocomposite hydrogel actuator with water-promoted thermal response, *Macromol. Rapid Commun.* 39 (2018), 1700863.
- [19] P. Tian, X. Gao, G. Wen, L. Zhong, Z. Wang, Z. Guo, Novel fabrication of polymer/carbon nanotube composite coated Janus paper for humidity stress sensor, *J. Colloid Interface Sci.* 532 (2018) 517–526.
- [20] T. Jia, Y. Wang, Y. Dou, Y. Li, M. Jung de Andrade, R. Wang, S. Fang, J. Li, Z. Yu, R. Qiu, Z. Liu, Y. Cheng, Y. Su, M. Minary-Jolandan, R.H. Baughman, D. Qian, Z. Liu, Moisture sensitive smart yarns and textiles from self-balanced silk fiber muscles, *Adv. Funct. Mater.* 29 (2019), 1808241.
- [21] J. Zhou, Y. Zhang, G. Jia, Z. Chen, Y. Yang, L. Zhang, A multifunctional sponge incorporated with  $\text{TiO}_2$  and graphene oxide as a reusable absorbent for oil/water separation and dye absorption, *New J. Chem.* 45 (2021) 4835–4842.
- [22] Z. Chen, Y. Zhang, Y. Yang, X. Shi, L. Zhang, G. Jia, Hierarchical nitrogen-doped holey graphene as sensitive electrochemical sensor for methyl parathion detection, *Sens. Actuators B Chem.* 336 (2021), 129721.

- [23] L. Wang, Y. Zhang, J. Zhang, X. Zhou, Preparation of an Au nanoparticle-graphene oxide quantum dot hybrid and its use in surface-enhanced Raman scattering, *New Carbon Mater.* 34 (2019) 606–610.
- [24] Y. Ge, R. Cao, S. Ye, Z. Chen, Z. Zhu, Y. Tu, D. Ge, X. Yang, A bio-inspired homogeneous graphene oxide actuator driven by moisture gradients, *Chem. Commun.* 54 (2018) 3126–3129.
- [25] Y. Qiu, M. Wang, W. Zhang, Y. Liu, Y.V. Li, K. Pan, An asymmetric graphene oxide film for developing moisture actuators, *Nanoscale* 10 (2018) 14060–14066.
- [26] W. Zhang, L. Wang, K. Sun, T. Luo, Z. Yu, K. Pan, Graphene-based Janus film with improved sensitive response capacity for smart actuators, *Sens. Actuators B Chem.* 268 (2018) 421–429.
- [27] M.F. Döpke, J. Lützenkirchen, O.A. Moulton, B. Siboulet, J.-F. Dufréche, J. T. Padding, R. Hartkamp, Preferential adsorption in mixed electrolytes confined by charged amorphous silica, *J. Phys. Chem. C* 123 (2019) 16711–16720.
- [28] C. Xiang, W. Wang, Q. Zhu, D. Xue, X. Zhao, M. Li, D. Wang, Flexible and super-sensitive moisture-responsive actuators by dispersing graphene oxide into three-dimensional structures of nanofibers and silver nanowires, *ACS Appl. Mater. Interfaces* 12 (2020) 3245–3253.
- [29] J. Wang, Y. Liu, Z. Cheng, Z. Xie, L. Yin, W. Wang, Y. Song, H. Zhang, Y. Wang, Z. Fan, Highly conductive MXene film actuator based on moisture gradients, *Angew. Chem. Int. Ed.* 59 (2020) 14029–14033.
- [30] J. Wu, P. Lu, J. Dai, C. Zheng, T. Zhang, W. Yu, Y. Zhang, High performance humidity sensing property of  $Ti_3C_2T_x$  MXene-derived  $Ti_3C_2T_x/K_2Ti_4O_9$  composites, *Sens. Actuators B Chem.* 326 (2021), 128969.
- [31] H. Tai, Z. Duan, Z. He, X. Li, J. Xu, B. Liu, Y. Jiang, Enhanced ammonia response of  $Ti_3C_2T_x$  nanosheets supported by  $TiO_2$  nanoparticles at room temperature, *Sens. Actuators B Chem.* 298 (2019), 126874.
- [32] G.S. Lee, T. Yun, H. Kim, I.H. Kim, J. Choi, S.H. Lee, H.J. Lee, H.S. Hwang, J. G. Kim, D.-W. Kim, H.M. Lee, C.M. Koo, S.O. Kim, Mussel inspired highly aligned  $Ti_3C_2T_x$  MXene film with synergistic enhancement of mechanical strength and ambient stability, *ACS Nano* 14 (2020) 11722–11732.
- [33] S. Huang, V.N. Mochalin, Hydrolysis of 2D transition-metal carbides (MXenes) in colloidal solutions, *Inorg. Chem.* 58 (2019) 1958–1966.
- [34] A. Catino, G. de Gennaro, A. Di Gilio, L. Facchini, D. Galetta, J. Palmisani, F. Porcelli, N. Varesano, Breath analysis: a systematic review of volatile organic compounds (VOCs) in diagnostic and therapeutic management of pleural mesothelioma, *Cancers* 11 (2019) 831.
- [35] H. Liao, X. Guo, P. Wan, G. Yu, Conductive MXene nanocomposite organohydrogel for flexible, healable, low-temperature tolerant strain sensors, *Adv. Funct. Mater.* 29 (2019), 1904507.
- [36] Z. Duan, Y. Jiang, M. Yan, S. Wang, Z. Yuan, Q. Zhao, P. Sun, G. Xie, X. Du, H. Tai, Facile, flexible, cost-saving, and environment-friendly paper-based humidity sensor for multifunctional applications, *ACS Appl. Mater. Interfaces* 11 (2019) 21840–21849.
- [37] H. Gu, Y. Xing, P. Xiong, H. Tang, C. Li, S. Chen, R. Zeng, K. Han, G. Shi, Three-dimensional porous  $Ti_3C_2T_x$  MXene–graphene hybrid films for glucose biosensing, *ACS Appl. Mater. Interfaces* 2 (2019) 6537–6545.
- [38] J. Yan, C.E. Ren, K. Maleski, C.B. Hatter, B. Anasori, P. Urbankowski, A. Sarycheva, Y. Gogotsi, Flexible MXene/graphene films for ultrafast supercapacitors with outstanding volumetric capacitance, *Adv. Funct. Mater.* 27 (2017), 1701264.
- [39] J. Zhang, Y. Zhang, J. Zhou, L. Wang, Construction of a highly sensitive non-enzymatic nitrite sensor using electrochemically reduced holey graphene, *Anal. Chim. Acta* 1043 (2018) 28–34.
- [40] P. Sambyal, A. Iqbal, J. Hong, H. Kim, M.-K. Kim, S.M. Hong, Y. Gogotsi, C.M. Koo, Ultralight and mechanically robust  $Ti_3C_2T_x$  hybrid aerogel reinforced by carbon nanotubes for electromagnetic interference shielding, *ACS Appl. Mater. Interfaces* 11 (2019) 38046–38054.
- [41] K.M. Kang, D.W. Kim, C.E. Ren, K.M. Cho, S.J. Kim, J.H. Choi, Y.T. Nam, Y. Gogotsi, H.-T. Jung, Selective molecular separation on  $Ti_3C_2T_x$ –graphene oxide membranes during pressure-driven filtration: comparison with graphene oxide and MXenes, *ACS Appl. Mater. Interfaces* 9 (2017) 44687–44694.
- [42] M. Lu, W. Han, H. Li, H. Li, B. Zhang, W. Zhang, W. Zheng, Magazine-bending-inspired architecting anti-T of MXene flakes with vertical ion transport for high-performance supercapacitors, *Adv. Mater. Interfaces* 6 (2019), 1900160.
- [43] L. Shi, Z. Ying, A. Xu, Y. Cheng, Unraveling the water-mediated proton conduction mechanism along the surface of graphene oxide, *Chem. Mater.* 32 (2020) 6062–6069.
- [44] C.-F. Du, Q. Liang, Y. Zheng, Y. Luo, H. Mao, Q. Yan, Porous MXene frameworks support pyrite nanodots toward high-rate pseudocapacitive Li/Na-ion storage, *ACS Appl. Mater. Interfaces* 10 (2018) 33779–33784.
- [45] R. Castaldo, G.C. Lama, P. Aprea, G. Gentile, V. Ambrogi, M. Lavorgna, P. Cerruti, Humidity-driven mechanical and electrical response of graphene/cloisite hybrid films, *Adv. Funct. Mater.* 29 (2018), 1807744.
- [46] J. He, P. Xiao, J. Zhang, Z. Liu, W. Wang, L. Qu, Q. Ouyang, X. Wang, Y. Chen, T. Chen, Highly efficient actuator of graphene/polydopamine uniform composite thin film driven by moisture gradients, *Adv. Mater. Interfaces* 3 (2016), 1600169.
- [47] T. Liu, X. Liu, N. Graham, W. Yu, K. Sun, Two-dimensional MXene incorporated graphene oxide composite membrane with enhanced water purification performance, *J. Membr. Sci.* 593 (2020), 117431.
- [48] Z. Duan, Y. Jiang, Q. Zhao, Q. Huang, S. Wang, Y. Zhang, Y. Wu, B. Liu, Y. Zhen, H. Tai, Daily writing carbon ink: novel application on humidity sensor with wide detection range, low detection limit and high detection resolution, *Sens. Actuators B Chem.* 339 (2021), 129884.
- [49] C. Chen, X. Wang, M. Li, Y. Fan, R. Sun, Humidity sensor based on reduced graphene oxide/lignosulfonate composite thin-film, *Sens. Actuators B Chem.* 255 (2018) 1569–1576.



**Guangwen Jia** is a M.S. candidate in the School of Materials Engineering at Shanghai University of Engineering Science. She received her bachelor's degree from HuaiBei Normal University in 2019. She works in Prof. Yan Zhang's group and current research interests focus on 2D materials for actuators.



**Ao Zheng** is currently a Ph.D. student in the Department of Prosthodontics, Shanghai Ninth People's Hospital, Shanghai Jiao Tong University School of Medicine; College of Stomatology, Shanghai Jiao Tong University; National Center for Stomatology; National Clinical Research Center for Oral Diseases; Shanghai Key Laboratory of Stomatology; Shanghai Engineering Research Center of Advanced Dental Technology and Materials and is supervised by Prof. Xinquan Jiang. Her research interests include the frontier research of oral hard tissue regeneration and biomaterials.



**Xiao Wang** is currently a Ph.D. student at the Shanghai Jiao Tong University School of Medicine, Shanghai Key Laboratory of Stomatology and Shanghai Research Institute of Stomatology (China) and is supervised by Prof. Xinquan Jiang. Her research focuses on prosthodontics and regenerative medicine, particularly on the bone regeneration and oral function restoration, with tissue engineering and regenerative medicine strategies.



**Lu Zhang** received his bachelor's degree from Shanxi Datong University, in 2019. She is currently pursuing her M.S. degree in Shanghai University of Engineering Science. Her current research interests focus on 2D materials for sensors.



**Ling Li** is a M.S. candidate in the School of Material Engineering, Shanghai University of Engineering Science. She received her bachelor's degree from Hengyang Normal University in 2020. She works in Prof. Yan Zhang's group and current research interests focus on the application of 2D materials for actuators.



**Chenxing Li** is a M.S. candidate in the School of Material Engineering, Shanghai University of Engineering Science. She received her bachelor's degree from Huainan Normal University in 2019. She works in Prof. Yan Zhang's group and current research interests focus on the application of 2D materials for water electrolysis.



**Lingyan Cao**, Ph.D., works as a assistant research fellow at Department of Prosthodontics, Shanghai Ninth People's Hospital, Shanghai Jiao Tong University School of Medicine; College of Stomatology, Shanghai Jiao Tong University; National Center for Stomatolgy; National Clinical Research Center for Oral Diseases; Shanghai Key Laboratory of Stomatolgy; Shanghai Engineering Research Center of Advanced Dental Technology and Materials. Her field of research is the frontier research of oral hard tissue regeneration, especially in the construction and application of bone tissue repair materials.



**Yan Zhang**, Ph.D., is an associated professor in the school of material engineering, Shanghai University of Engineering Science. She received her Ph. D. degree from Shanghai Jiao Tong University in 2013. Now, her research focuses on 2D materials for sensors and actuators.